Hybrid Detectors Based on Selective Endmembers

Liangpei Zhang, Bo Du, and Yanfei Zhong

Abstract—Subpixel target detection is a challenge in hyperspectral image analysis. As the spatial resolution of hyperspectral imagery is usually limited, subpixel targets only occupy part of the pixel area. In such cases, the spatial characteristics of the targets are hard to acquire, and the only information we can use comes from spectral characteristics. Several kinds of method based on spectral characteristics have been proposed in the past. One is the linear unmixing method, which can provide the abundances of different endmembers in the hyperspectral imagery, including the target abundance. Another focuses on providing statistically reliable rules to separate subpixel targets from their backgrounds. Recently, hybrid detectors combining the aforementioned two methods were put forward, which cannot only figure out the quantitative information of the endmembers but also put this quantitative information into an adaptive matched subspace detector or adaptive cosine/coherent estimate detector to separate the target pixels from the background with statistically reliable rules. However, in these methods, all the endmembers are used to construct the statistical rule, while in most cases only some of the endmembers are actually contained in the pixels. This paper proposes hybrid endmembers selective detectors in which different kinds of endmembers are used according to different pixels to ensure that the true composition of endmembers in each pixel is applied in the detection procedure. Three different types of hyperspectral data were used in our experiments, and our proposed hybrid endmember selective detectors showed better performances than the current hybrid detectors in all the experiments.

Index Terms—Fully constrained least squares (FCLS), hyperspectral data, linear mixture models (LMMs), target detection.

I. INTRODUCTION

SPECTRAL imaging, airborne or spaceborne, can acquire data with a wide spatial coverage of ground objects with a much larger spectral range and a much higher spectral resolution than is possible with multispectral sensors. Therefore, the ability to detect individual features or objects is dramatically better than with multispectral imagery, particularly when the spectral differences of the materials are minor. However, due to the limitations of the spatial resolution of hyperspectral imagery, the targets are often smaller than the pixel size and resolved within a pixel. In such cases, the targets are called subpixel targets. Subpixel target detection is very important in civil and military applications, such as agricultural yield estimation, mineral exploration, fire monitoring, battleground reconnaissance, and so on.

The existing subpixel target detection methods mainly depend on the spectral characteristics of the targets to be detected [1]–[6]. One kind of subpixel detection method is the linear unmixing (LU) analysis methods. These methods are based on the linear mixture model (LMM), in which a pixel's spectrum is assumed to be composed of several pure materials' spectra, called endmembers. In this model, pixels in the imagery are called mixed pixels, and the signal of a mixed pixel is the sum of the different endmembers' spectral signals. Different endmembers' weighted values are assigned according to their fractions in the pixel. This model is based on the assumption that the signals acquired by the sensor are reflected directly from the ground objects' surfaces, not reflected twice or more times by surfaces on the ground. If multiple reflections are taken into consideration, the LMM has to be extended into a nonlinear model. However, the LMM is suitable in most cases, and it has clear physical meaning. Based on LMM, several spectral LU methods were developed [7]–[15]. Among them, the fully constrained least squares (FCLS) method is one that has been successfully used in subpixel target detection. In this method, two constrained conditions are used: each endmember's abundance is nonnegative and all the endmembers' abundances in each pixel sum to one. With these two constraining conditions, the abundance results have physical meanings and can be weighted as the percentages of different materials in each pixel. In this method, the subpixel target is assumed as an endmember in the imagery and its percentage in each pixel is figured out by the least squares estimation (LSE) method [10]. In this way, a quantitative detection result is determined.

Another kind of subpixel target detection method is based on a statistical hypothesis test. Adaptive matched subspace detector (AMSD) is such an algorithm that formulates the target and background subspaces and uses the LMM and the generalized likelihood ratio (LR) approach to separate a probable subpixel target [16], [17]. The key factor in AMSD is the target abundance and the noise variance, which can be estimated by the maximum likelihood (ML) method, and with which a Neyman–Pearson detector can be designed to maximize the probability of detection for a certain given false alarm probability. Due to the complexity of the changes in atmospheric conditions, sensor geometry, surface defects, and films, target variability is not negligible and can have an impact on the detection result. However, by the use of the subspace model, AMSD can resolve the problem and provides a reliable rule to separate the target pixels from nontarget ones.

Adaptive cosine/coherent estimate (ACE) is another statistical hypothesis test-based method [3], [18]. Unlike AMSD, ACE assumes no structured background. Instead, ACE models the background as a multivariate normal distribution. ACE discards both the sum to one constraint and the nonnegative constraint.

The authors are with the State Key Laboratory of Information Engineering in Surveying, Mapping and Remote Sensing, Wuhan University, Wuhan 430079, China (e-mail: zlp62@public.wh.hb.cn; gunspace@163.com; zhongyanfei@lmars.whu.edu.cn).

This characteristic allows it to provide a better separability between targets and background as the target abundance can be fully expressed by a large enough value.

Recently, hybrid subpixel target detection methods have been proposed, which combine the advantages of LU-based methods and statistical hypothesis test-based methods [19]. Hybrid detectors model the background with both physically meaningful abundance and the statistical hypothesis test. In this way, the background is better characterized and the separability of targets and background is improved. In [19], Broadwater and Chellappa used FCLS, AMSD, and ACE to develop two hybrid detectors. Compared to the aforementioned two kinds of method, the two hybrid methods proved to be less sensitive to the number of endmembers used, and provided a better separability and improved receiver operating characteristic (ROC) curves [19], [20].

All the aforementioned methods use a fixed number of endmembers in the formulation of the background model. However, in reality, not all the pixels contain all the endmembers. In fact, in most cases, many pixels contain only some of the endmembers. Thus, it is natural to formulate the background structure with the actual kinds of endmembers. This paper develops the aforementioned two hybrid detectors into a novel version with actual endmembers. With better formulated background structures, they are expected to have a better performance. The rule for choosing the true kinds of endmembers is obviously the key factor in the procedure. A cross-correlogram spectral matching (CCSM) technique is used to determine the true kinds of endmembers of the individual pixel. The technique focuses on evaluating the similarity between the endmember's signal and the pixel's signal by computing their response value. It is used to find the orthogonal response signal that is in accordance with an endmember, since the endmembers' signals are independent of each other. Our hypothesis is that with true kinds of endmembers, the better formulated background structure combined with a physical meaningful LMM and statistical hypothesis test can provide a higher separability between targets and background.

The remainder of this paper is organized as follows. The current hybrid algorithms are described in Section II. Section III describes our proposed hybrid selective endmembers detectors. Section IV details the experiments used to test our hypothesis and presents the results of the experiments showing that the hybrid detectors excel in these areas: endmember insensitivity, the ability to increase the separation between targets and background, and improved ROC performance over multiple images. Section V summarizes this paper.

II. CURRENT HYBRID DETECTORS

A. LMM

Several analytical models for the mixing of different materials have been proposed [21] among which the LMM is the most widely used one, and it is the basis of current hybrid detectors. All the models, however, assume that within a certain scene, the surface is dominated by a limited number of distinct substances, each of which has a relatively constant spectrum. Here, the substances and their according fraction are called endmembers and fractional abundances, respectively. Suppose that the scene area of a pixel is divided proportionally according to the fractional abundances of the endmembers in the scene area. Moreover, the reflected radiation signals received in the sensor are from the scene area after only one reflection. Then, the reflected radiation of the pixel will convey the characteristics of these endmembers with the corresponding proportions. In this sense, there exists a linear relationship between the fractional abundance of the substances comprising the area being imaged and the spectra in the reflected radiation [22]. Therefore, the spectrum of such a mixed pixel is composed of different endmembers, which are the pure spectra of certain materials. The spectrum signature of an observed mixed pixel is expressed as

$$\mathrm{x} = \mathrm{M}\alpha + n \qquad (1)$$

where M is the endmember signature matrix composed of $[\mathrm{m}_1 \mathrm{m}_2, \ldots, \mathrm{m}_j, \ldots, \mathrm{m}_p]$, and m_j is an $l \times 1$ column vector representing the jth endmember in the image scene. $\alpha = (\alpha_1, \alpha_2, \ldots, \alpha_p)^{\mathrm{T}}$ is a $p \times 1$ abundance column vector, which is composed of each endmember's abundance in an observed pixel. n is a $l \times 1$ noise vector. l is the band number of the image and p is the number of endmembers in the image.

To make the LMM have physical meaning, two constraints are defined: the abundance nonnegative constraint (ANC) and the abundance sum-to-one constraint (ASC).

$$\sum_{j=1}^{P} \alpha_j = 1 \qquad (2)$$

$$\alpha_j \geq 0 \qquad \text{for } 1 \leq j \leq p. \qquad (3)$$

The ANC and ASC constraints only hold for physically meaningful endmembers. For example, the AMSD algorithm proposed for hyperspectral imagery by Manolakis [9] does not use such physical endmembers. With these two constraints, the linear mixture spectrum analysis methods can extract the exact abundances of endmembers in different mixed pixels. For example, the FCLS separates the different endmembers' abundances by the least squares method. The abundance information is useful in the estimation of different materials in the scene. However, for the target detection domain, the exact estimation of abundances is not so necessary. In fact, the target detection task focuses on the separation of target and background. However, the information extracted by the linear mixture spectrum analysis methods does give a basis for further separation analysis.

B. FCLS

There are two ways to implement the FCLS. One is to impose the ANC after the SCLS (sum-to-one constrained least squares) called normalized SCLS, or by imposing the ASC after NCLS (nonnegatively constrained least squares) called normalized NCLS [23], [24]. The second is to execute both the constraints simultaneously [25]. It has been shown in [26] that relative to the former way, the latter produces a more optimal solution. In this paper, we carry out the latter in which FCLS is developed from the nonnegativity constrained least squares (NCLS) method. Neither FCLS nor NCLS produce a closed-form solution, but they do provide a reliable numerical solution.

In FCLS, the endmember matrix M mentioned in the previous section is added with a new dimension and thus is expressed as

$$N = \begin{bmatrix} \sigma M \\ 1^T \end{bmatrix}$$

where $1 = (1, 1, \ldots, 1)^T$ is a $p \times 1$ vector and the pixel signal is expressed accordingly as

$$s = \begin{bmatrix} \sigma r \\ 1 \end{bmatrix}.$$

Within the aforementioned expression, the parameter σ controls how close the resulting abundances would sum to one. The smaller the parameter, the closer the result is to the physical reality but with a slower convergence rate. After the aforementioned procedure is introduced into the NCLS, the FCLS equals the following optimal problem:

$$\text{Minimize LSE} = (N\alpha - s)^T (N\alpha - s) \text{ over } \alpha$$

$$\text{subject to } \alpha > 0. \tag{4}$$

The key solution to the aforementioned problem involves Lagrange multipliers. We define a cost function J as

$$J = \frac{1}{2}(N\alpha - s)^T(N\alpha - s) + \lambda(a - c). \tag{5}$$

Let $a = c$, and $(\partial J / \partial \alpha)|_{\hat{\alpha}\text{FCLS}} = 0$
Then, we obtain

$$\hat{\alpha}_{\text{FCLS}} = (N^T N)^{-1} N^T s - (N^T N)^{-1} \lambda$$

$$= \hat{\alpha}_{LS} - (N^T N)^{-1} \lambda \tag{6}$$

$$\lambda = N^T (s - N\hat{\alpha}_{\text{FCLS}}). \tag{7}$$

As shown in [13], iterating the aforementioned two equations gives the solution to (4). Moreover, only when the Lagrange multiplier vector satisfies the Kuhn–Tucker conditions can the optimal solution to the aforementioned problem be found. In order to satisfy the condition, two index sets are formulated in the FCLS solution. One is named positive set R containing all indices (Lagrange multipliers) corresponding to positive components in the estimate $\hat{\alpha}_{LS}$, which can be computed by the least squares projection method in [26] and [27]. The least squares estimate of abundance $\hat{\alpha}$, $\hat{\alpha}_{LS}$ is expressed as

$$\hat{\alpha}_{LS} = (N^T N)^{-1} N^T s. \tag{8}$$

The other set is called active set P, which consists of all indices corresponding to negative and zero components in the estimate $\hat{\alpha}_{LS}$. Then, the Kuhn–Tucker conditions are defined as

$$\lambda_j = 0, \qquad j \in P \tag{9}$$

$$\lambda_j < 0, \qquad j \in R. \tag{10}$$

Iterating (6) and (7) until all the Lagrange multipliers in the passive set are zero and all Lagrange multipliers in the active set are either zero or negative, the Kuhn–Tucker conditions are then satisfied. In this way, an optimal mean-squared error solution for the unmixing of the image can be obtained.

C. Hybrid Detector With Structured Background

In order to formulate the structured background, the LMM is separated and a series of hypothesis is built

$$H_0 : x = B\alpha_{b,0} + n$$

$$H_1 : x = S\alpha_s + B\alpha_{b,1} + n \tag{11}$$

where the hypotheses H_0 and H_1 are according to the absence of the target and the presence of the target, respectively. B is a $L \times P'$ matrix representing the P' background endmembers' spectra, while S is a $L \times Q$ matrix representing the Q targets' spectra. Thus, M is the concatenation of S and B. In the hypotheses H_0, P' equals p and in the hypotheses H_1, $P' + Q = p$. In this way, the pixels containing the target spectrum and the ones solely containing the background spectrum are separated.

In addition, in this model the noise is assumed as a zero-mean normal distribution with covariance matrix $\sigma^2 I$. Then, the hypotheses are expressed as

$$H_0 : x \sim \tilde{N}\left(B\alpha_{b,0}, \sigma^2_{w,b}I\right)$$

$$H_1 : x \sim \tilde{N}\left(S\alpha_s + B\alpha_{b,1}, \sigma^2_w I\right). \tag{12}$$

With known noise variance σ^2_w and abundance vector α, we can use the LR method to formulate a Neyman–Pearson detector, which maximizes the probability of detection under a given probability of false alarm. However, in practice, these variables are usually unknown and are estimated from the image data by the ML method. The estimation of σ^2_w and α can be obtained using the same method as in FCLS [9].

$$\hat{a} = (M^T M)^{-1} M^T x = P_M x \tag{13}$$

$$\hat{\sigma}^2_w = \frac{1}{L - P} SSE(\hat{a}) \tag{14}$$

where

$$SSE(\hat{\alpha}) = \|e\|^2 = x^T x - \hat{x}^T \hat{x}$$

$$= x^T (I - P_M) x = x^T P'_M x \tag{15}$$

$$P_M = M(M^T M)^{-1} M^T \tag{16}$$

L band number
P endmember number

Then, by the use of the LR method, a Neyman–Pearson detector maximizing the detection probability under a given false alarm probability is designed [28]

$$\text{GLR}(x) = \frac{L_1(.)}{L_0(.)} = \frac{L\left(\hat{\alpha}, \sigma^2_w; x\right)}{L\left(\hat{\alpha}_b, \sigma^2_{w,b}; x\right)} = \left(\frac{x^T P'_B x}{x^T P'_M x}\right)^{L/2}. \tag{17}$$

We have to define a threshold η' to decide on the hypothesis H_1 when $\text{GLR}(x) > \eta'$, or the hypothesis H_0 otherwise. The Neyman–Pearson detector has a constant false alarm rate (CFAR) property. In this sense, the threshold η' decides the detection probability and the false alarm probability. In order to determine η', the probability distribution of $\text{GLR}(x)$ has to be determined. As GLR(x) is a nonnegative, monotonically increasing function, we drop the L/2 power and subtract ONE

from it, which does not change its outcome. Then, we get the adaptive subspace matched detector (AMSD)

$$T_{\text{AMSD}}(x) = \frac{x^{\text{T}}\left(P_B' - P_M'\right)x}{x^{\text{T}}P_M' x} \tag{18}$$

$$P_B' = I - P_B = I - B(B^{\text{T}}B)^{-1}B^{\text{T}}. \tag{19}$$

This expression of (18) does not change the effect of the output of (17). However, the distribution of the adaptive subspace matched detector (AMSD) is much easier to determine, since the numerator and denominator are independent.

$$T_{\text{AMSD}}(x) \sim F_{P, L-P-Q}\left(\frac{\|P_B' S\alpha_S\|^2}{\sigma^2}\right). \tag{20}$$

Of course, the test data are assumed to have a multivariate normal distribution. There are several methods to evaluate the normality and correlation properties of vector data, such as multivariate techniques for evaluating joint normality, and techniques using unidimensional projections of multivariate data [29]

The hybrid structured detector (HSD) uses the same structured background but substitutes the endmembers and the estimation of their respective abundances with the real endmembers and their abundances from the FCLS method. In this case, the HSD uses the following hypotheses:

$$H_0 : x \sim N\left(\text{B}\alpha_{b,0}, \sigma_0^2\Gamma\right)$$
$$H_1 : x \sim N\left(\text{S}\alpha_s + \text{B}\alpha_{b,1}, \sigma_1^2\Gamma\right). \tag{21}$$

The noise is Gaussian with covariance $\sigma^2\Gamma$. With this covariance matrix, the likelihood hypothesis is formulated as in ACE, given in the next section.

$$L(x, Y|H_0) = (2\pi)^{-\frac{1}{2}L(N+1)}|\Gamma|^{-\frac{1}{2}(N+1)}\left(\sigma_0^2\right)^{-\frac{1}{2}L}$$
$$\cdot \exp\left\{-\frac{(x - \text{B}a_{b,0})^{\text{T}}\Gamma^{-1}(x - \text{B}a_{b,0})}{2\sigma_0^2}\right.$$
$$\left. -\frac{1}{2}\sum_{i=1}^{N} y_i^{\text{T}}\Gamma^{-1}y_i\right\} \tag{22}$$

$$L(x, Y|H_1) = (2\pi)^{-\frac{1}{2}L(N+1)}|\Gamma|^{-\frac{1}{2}(N+1)}\left(\sigma_1^2\right)^{-\frac{1}{2}L}$$
$$\cdot \exp\left\{-\frac{(x - \text{E}a)^{\text{T}}\Gamma^{-1}(x - \text{E}a)}{2\sigma_1^2}\right.$$
$$\left. -\frac{1}{2}\sum_{i=1}^{N} y_i^{\text{T}}\Gamma^{-1}y_i\right\} \tag{23}$$

where $\Gamma = (1/N)\sum_{i=1}^{N} y_i y_i^{\text{T}}$. y_i ($1 \leqslant i \leqslant N$) is a set of training background pixels, which are independently and identically distributed. $\text{E}a$ is the concatenation of the appropriate $\text{S}a_s$ and $\text{B}a_{b,1}$ spaces. To avoid confusion, we use E to stand for the whole endmember matrix in the following text.

The variance estimations under the individual hypotheses are

$$\widehat{\sigma}_0^2 = \frac{1}{L}(x - \text{B}a_{b,0})^{\text{T}}\Gamma^{-1}(x - \text{B}a_{b,0}) \tag{24}$$

$$\widehat{\sigma}_1^2 = \frac{1}{L}(x - \text{E}a)^{\text{T}}\Gamma^{-1}(x - \text{E}a). \tag{25}$$

The abundance estimations are obtained by the FCLS algorithm mentioned before. However, with the new covariance matrix, the new iterating equations are where

$$\widehat{a} = (\text{E}^{\text{T}}\Gamma^{-1}\text{E})^{-1}\text{E}^{\text{T}}\Gamma^{-1}x - (\text{E}^{\text{T}}\Gamma^{-1}\text{E})^{-1}\lambda \tag{26}$$
$$\lambda = \text{E}^{\text{T}}\Gamma^{-1}(x - \text{E}\widehat{a}). \tag{27}$$

We substitute all the aforementioned estimations into (22) and (23). Then, the hybrid detector based on structured background, or HSD, can be derived from the traditional AMSD

$$D_{\text{HSD}}(x) = \frac{\left(x - \text{B}\widehat{a}_b'\right)^{\text{T}}\Gamma^{-1}\left(x - \text{B}\widehat{a}_b'\right)}{(x - \text{E}\widehat{a}')^{\text{T}}\Gamma^{-1}(x - \text{E}\widehat{a}')}. \tag{28}$$

D. Hybrid Detector With Unstructured Background

The hybrid detector with unstructured background, or the hybrid unstructured detector, is derived from the adaptive cosine/coherent (ACE) detector. In this algorithm, the background is not structured but modeled as a statistical distribution, usually the multivariate normal distribution. It removes all the background structure information by setting $B = 0$. In addition, the background is assumed to be a zero-mean Gaussian distribution with a covariance Γ_b. However, the HSI data often have a nonzero mean, so we remove the estimated mean to comply with this assumption. The according hypotheses are

$$H_0 : x \sim N(0, \Gamma_b)$$
$$H_1 : x \sim N(\text{S}\alpha_s, \Gamma_b). \tag{29}$$

In order to obtain the ML estimation of the covariance matrix, it is assumed that a set of training pixels with independent and identical distributions are available and that the training pixels x(n) and the test pixel x are also statistically independent. Then, following the work of Kelly [30], [31], by the way of a generalized LR method, we obtain

$$D_K(x) = \frac{x^{\text{T}}\widehat{\Gamma}_b^{-1}S\left(S^{\text{T}}\widehat{\Gamma}_b^{-1}S\right)^{-1}S^{\text{T}}\widehat{\Gamma}_b^{-1}x}{N + x^{\text{T}}\widehat{\Gamma}_b^{-1}x} \tag{30}$$

where $\widehat{\Gamma}_b = (1/N)\sum_{n=1}^{N} x(n)x^{\text{T}}(n)$ and is the ML estimation of the covariance matrix. N is the number of training background pixels in the image. In addition, a threshold η_A is also defined. Then, we decide on the hypothesis H_1 if $D_K(x) > \eta_A$, and the hypothesis H_0 otherwise. This threshold determines both detection probability P_D and false alarm probability P_{FA}. The matrix S consists of the targets' spectra in the target subspace. When the dimension of target subspace P increases to L (band number of the data), the matrix S becomes full rank and thus invertible. Therefore, we only need to find deterministic targets in the data subspace and (30) is simplified to

$$D_K(x) = x^{\text{T}}\widehat{\Gamma}_b^{-1}x. \tag{31}$$

This detector was derived first by Kelly and Forsythe [32], and its theory is similar to that of Reed and Xiaoyu [33], who also use the Mahalanobis distance between the test pixel and the mean of the background. This detector has been a widely used algorithm in anomaly detection [34], which is not the domain of this paper. Like the anomaly detection algorithms,

a key assumption of (29) is that the covariance matrices of the background in the two hypotheses are the same. However, as to the subpixel targets, the background of the two hypotheses are different. In this case, the two hypotheses are expressed as

$$
\begin{aligned}
H_0 &: x = b \\
H_1 &: x = Sa_S + \sigma b.
\end{aligned} \tag{32}
$$

Therefore, the backgrounds of the two hypotheses have the same covariance structure but different variances: $x \sim \tilde{N}(0, \sigma_0^2 \Gamma_b)$ according to hypothesis H_0 and $x \sim \tilde{N}(Sa_S, \sigma_1^2 \Gamma_b)$ according to hypothesis H_1. The abundance and covariance are estimated by MLE

$$
\widehat{a}_s = \left(S^T \Gamma_b^{-1} S\right)^{-1} S^T \Gamma_b^{-1} x \tag{33}
$$

$$
\widehat{\sigma}_0^2 = \frac{1}{L} x^T \Gamma_b^{-1} x \tag{34}
$$

$$
\widehat{\sigma}_1^2 = \frac{1}{L} (x - Sa_S)^T \Gamma_b^{-1} (x - Sa_S). \tag{35}
$$

Then, we obtain the ACE detector, by the GLR method [28], [29].

$$
D_{\text{ACE}}(x) = \frac{x^T \widehat{\Gamma}_b^{-1} S \left(S^T \widehat{\Gamma}_b^{-1} S\right)^{-1} S^T \widehat{\Gamma}_b^{-1} x}{x^T \widehat{\Gamma}_b^{-1} x}. \tag{36}
$$

Considering the hypothesis H_0, $D_{\text{ACE}}(x)$ fits the distribution as

$$
D_{\text{ACE}}(x) \sim Beta\left(\frac{P}{2}, \frac{L-P}{2}\right)
$$

where P and L have the same meaning as before. Since the ACE statistic depends only on P and L, it also has the CFAR property. Furthermore, we can find a threshold to determine the false alarm rate for the CFAR detection.

By simply replacing the abundances estimations with the abundances from the FCLS, we can obtain the ACE-based hybrid unstructured detector

$$
D_{\text{HUD}}(x) = \frac{x^T \widehat{\Gamma}_b^{-1} Sa_S'}{x^T \widehat{\Gamma}_b^{-1} x} \tag{37}
$$

where a_S' is a replacement for a_S, and $a_S = (S^T \widehat{\Gamma}_b^{-1} S)^{-1} S^T \cdot \widehat{\Gamma}_b^{-1} x$. a_S' is obtained by using FCLS to calculate all the abundances $a' = [a_S'\ a_B']$, concatenation of the target and background abundances.

III. HYBRID DETECTORS BASED ON SELECTIVE ENDMEMBERS

Both of the aforementioned hybrid algorithms use a fixed number of endmembers in the formulation of the detectors. In the HSD, the background structure is composed of a fixed number of endmembers for each pixel in the imagery and the abundances are also extracted using a fixed number of endmembers. Accordingly, the detection strategy is constructed by the fixed number of endmembers and their abundances. In the unstructured background hybrid algorithm, the abundances $\widehat{a}$, which is the replacement for a, also comes from FCLS with a fixed number of endmembers. However, it has been shown that, in most cases, the individual pixel contains only some of

the whole endmember set. In fact, Chang and Du [35] revealed that most of the pixels in the imagery usually contain only some of the endmembers. Therefore, the traditional fixed endmember analysis can violate the actual structural composition of the pixels. The redundant endmembers may then seriously affect the extraction of the endmembers' abundances. In the structured hybrid detector, the structure of the background using the wrong kinds of endmembers cannot represent the real relationship of the endmembers in the scene and thus decreases the separability of targets and background. In the unstructured hybrid detector, although the removal of background structure with ASC and ANC enhances the separability of target and background, the plausible abundances of endmembers coming from conventional FCLS, which has both constraints but fixed endmembers, may also counteract its effort.

In this case, we use a dynamic selection strategy for endmembers to develop hybrid detectors based on selective endmembers. In [36], D. A. Robert proposed a multiple endmember spectral mixture analysis, which focuses on accurately estimating the abundances of the endmembers by dynamically selecting optimal endmembers for each pixel from an endmember data set before unmixing. In our method, the real composition of endmembers in each pixel is extracted, and this endmembers selection information is introduced into the current hybrid detectors. Then, the new formulated HSD can represent the composition of endmembers in each pixel as truly as possible. In addition, the new formulated hybrid unstructured detector also uses the endmember abundances that tally better with the actual situation. The aforementioned strategy aims at increasing the separability of targets and background.

Given that we have a full set of endmembers in the scene, a straightforward method of identifying the endmember kinds in a pixel is by an examination of all the possible combinations of endmembers and the optimal one is that with the least residual error. However, it is obvious that as the number of endmembers increases, the number of combinations would become so large that the computational burden would become unacceptable. In this paper, we use the theory of the CCSM technique to identify the proper subset of endmembers according to the real composition in the scene. The CCSM technique was first proposed by Meer and Bakker [37] and was used in mineralogical mapping applications. It provides a statistical measure for the spectral similarity between a known reference material (either a laboratory spectrum or a pixel spectrum from the imagery to represent the material of interest) and an unknown material underlying a pixel. The cross correlation is calculated at different matching positions by moving the reference spectrum over m channels to the shorter wavelength end or to the longer wavelengths. In this paper, we follow the theory of the CCSM but only compute the cross correlation at the matching position 0. We propose a process to extract the endmembers in each pixel of the scene and introduce information on the kinds of endmembers to the traditional hybrid detectors. The procedure for extracting the kinds of endmembers is as follows.

1) Given the full set of endmembers of the scene, we calculate the cross correlations between the test pixel and each of the endmembers in the set

$$
r = \frac{n \sum R_r R_t - \sum R_r \sum R_t}{\sqrt{[n \sum R_r^2 - (\sum R_r)^2] \cdot [n \sum R_t^2 - (\sum R_t)^2]}} \tag{38}
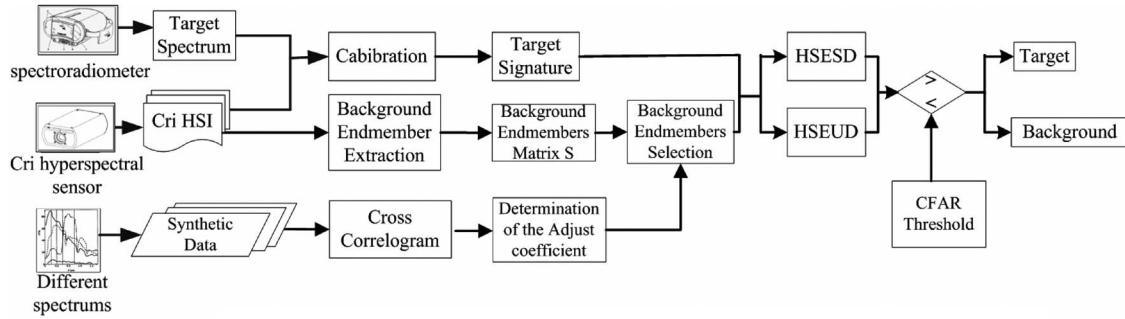$$

Fig. 1. Computational structure of the hybrid selective endmembers detectors.

where R_r is the reference spectrum or endmember signal that accords to each column of M in (1) and R_t is the test spectrum, which accords to the observed pixel x in (1). n is the number of overlapping positions and equals the number of spectral bands at the matching position 0.

2) The endmember having the largest cross correlation is chosen as the preferred one.

3) The influencing factors of the chosen endmembers are subtracted from the test pixel spectrum signal as follows, to obtain the remaining test pixel spectrum signal:

$$x_r = x - r_{\max} A_{\max} \qquad (39)$$

where $A_{\max}$ is the largest endmember and $r_{\max}$ is its corresponding effect in the pixel. x_r is the residual signal after the subtraction.

However, for the algorithm's flexibility, we add an adjustment coefficient η, and the remaining test pixel spectrum signal is expressed as

$$x_r = x - \eta r_{\max} A_{\max} \qquad (40)$$

where η controls the weight of the endmember in the pixel spectrum signal. It adjusts the endmembers to a suitable scale to reflect their real proportion in order to extract the right kinds of endmembers. We confine it in [0, 1]. In our experiments, we used synthetic data first with known kinds of endmembers to figure out the optimal numerical range of η. It was then used in the detection experiments that followed.

4) The cross correlations were calculated between the remaining test pixel spectrum signal and the endmembers, except for the selected ones.

5) Steps 2) to 4) were repeated. The terminal conditions are that one component of x_r is negative or the change after subtraction is minor. Then, we have obtained all the selective endmember kinds in each pixel.

After the aforementioned procedure, we can get the full endmember matrix E_S and background endmember matrix B_S for each pixel, which are only comprised of those endmembers selected from the endmember matrix that are particular to the pixel under test. Then, we can introduce the matrices E_S and B_S into the HSD and the hybrid unstructured detector. The hybrid selective endmembers structured detector (HSESD) is formulated as

$$D_{\mathrm{HSESD}}(x) = \frac{(x - B_S a_{BS})^{\mathrm{T}} \Gamma^{-1}(x - B_S a_{BS})}{(x - E_S a_S)^{\mathrm{T}} \Gamma^{-1}(x - E_S a_S)} \qquad (41)$$

where a_S is the abundance vector according to the selected endmembers matrix E_S, and a_{BS} is the corresponding abundance vector of B_S.

Using the dynamic matrices E_S for each pixel in FCLS, we can also get more accurate abundances vector a_{TS} of the targets endmembers. Therefore, we replace the abundance in equation (37) with a_{TS} and get the hybrid selective endmembers unstructured detector (HSEUD)

$$D_{\mathrm{HSEUD}}(x) = \frac{x^{\mathrm{T}} \widehat{\Gamma} \widehat{q}_b^{-1} S a_{TS}}{x^{\mathrm{T}} \widehat{\Gamma}_b^{-1} x}. \qquad (42)$$

The computational structure of the implementation of the HSEDs is shown in Fig. 1.

IV. EXPERIMENT AND ANALYSIS

A. Data Description

Three kinds of data are used in our experiments.

1) Synthetic data: composed of several kinds of typical ground objects' spectra from the ENVI software library. This data are used to determine the value of the adjustment coefficient η in the endmembers kind extraction procedure. The adjustment of η is simple as we have exact information on the targets and the composition of endmembers in each pixel before detection. The formulation of this synthetic data is described in detail in Section IV-C.

2) Simulated data: composed of real-world hyperspectral imagery with added targets' spectra in some pixels. This imagery was the PHI imagery taken of the Changzhou area, China. For the convenience of subpixel target detection, the targets are spectra of typical ground objects in the same imagery, and they are added to certain pixels with a determined percentage. In the experiment, the spectrum of cement is selected as the target's signature to be added in 100 pixels, and the original signature in these pixels would be taken as background and reduced accordingly. The 100 pixels are divided into ten groups according to their target's abundance. The first group of pixels has 10% target and 90% background. The second group has 20% target and 80% background. The third group has 30% and 70%. Similarly, the abundance of target increases to 100% in steps of 10% and the abundance of background decreases to 0% in steps of 10%, as the group number increases to ten. The 100 targets are placed in ten columns with each column of ten targets at the same position. The positions of these targets are shown in Fig. 2 and denoted by white circles.
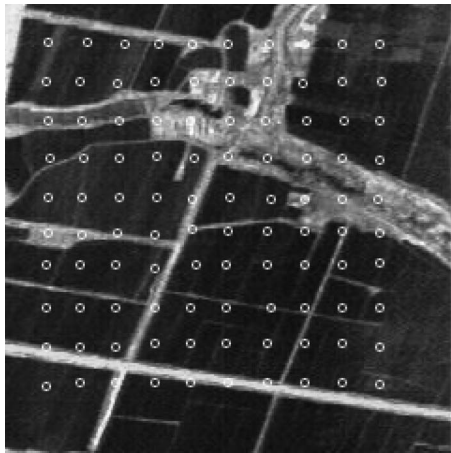
Fig. 2. PHI image in our experiments.

TABLE I
DETAILS OF THE IMAGES

Image	Background	Targets type	Color	Fill Factor	Target Number
1	Bare soil, grass, dry grass	Plastic	Green	20%	4
				40%	4
				80%	2
2	Bare soil, grass, dry grass	Metal	White	20%	4
				40%	4
				80%	4
3	Bare soil, grass, dry grass	Plastic	Green	20%	4
				40%	4
				80%	4
		Metal	White	20%	4
				40%	4
				80%	4
4	Bare soil, grass, dry grass	Stone	Grey	20%	4
				40%	4
				80%	2
5	Soil, cement	Metal	White	20%	4
				40%	4
				80%	2
6	Soil, cement	Plastic	Green	20%	4
				40%	4
				80%	2

3) *Real-world hyperspectral data:* The real-world hyperspectral data were acquired by the Nuance Cri hyperspectral sensor. This sensor can acquire imagery with a spectral resolution of under 10 nm, which is very suitable for hyperspectral imagery. Its spectral imaging scope covers 650 to 1100 nm. The imaging spatial range of the sensor is not so wide, so we use a small scale scene with comparatively smaller targets in the acquisition of Cri data. Moreover, to test the generality of the proposed algorithms, we acquired Cri imagery with different targets in different backgrounds. The details of the Cri data are listed in Table I, and the imagery of Cri data is shown in Fig. 3. There are three kinds of target and two kinds of background, and the detailed information about targets and background is also listed in Table I. The fill factors of different targets are also presented in the table with the number of targets present in the last column.

The PHI hyperspectral imagery covers a large area and contains a variety of endmembers. This point is in accordance with practical applications. Furthermore, a plentiful number of endmembers is necessary in the imagery to analyze endmember sensitivity. However, there were insufficient suitable subpixel targets. Therefore, the subpixel targets were simulated by adding targets' spectra into certain pixels with a known abundance. In addition, a series of data sets of Cri hyperspectral imagery was also used to enhance the evaluation of the methods in our experiments. These data sets were imaged in different real-world scenes where we had positioned enough subpixel targets and these data can be considered as real-world data. Moreover, these subpixel targets have known scales and there are plenty of them, which makes the quantitative comparison between different methods possible. However, these Cri images actually have fewer ground objects (according to many endmembers) than the PHI data. That is why we used both PHI data and Cri data in our experiments.

B. Background Endmembers and Target Signature Estimation

The proposed hybrid selective endmembers detectors require the estimation of background endmembers. However, in actual application, we cannot find the background endmembers in advance. There have been several commonly accepted methods to estimate the endmembers such as IEA, N-Finder, PPI, CCA, and so on [38], [39]. There is literature presenting these different methods' effects in detail. In order to make our new hybrid detectors comparable with the current hybrid detectors, we followed the work of Broadwater and Chellappa and used a developed IEA method proposed by Neville *et al.* [40].

As to the estimation of target signature, the three kinds of data have different cases. The synthetic data and simulated data contain the targets' spectrum signatures. For the real-world Cri data, as we could visit the imaging scene, we can easily determine the position of targets in the imagery and furthermore select the targets' spectrum signatures directly from the imagery. However, due to the targets' subpixel scale, it is not easy to select the pure spectrum signature from the imagery. In this case, we also measured the targets' spectra in the imaging scene by FieldSpec Pro spectroradiometer. This spectroradiometer is portable and can collect the spectrum of a wide range of ground object, including those in the near-infrared, visible, and midinfrared. Since the Cri sensor only covers a range between 650 and 1100 nm, the corresponding imagery has digital numbers in certain wavelengths. Therefore, we resampled the spectrum signature of the targets measured to the matching positions in the spectrum. Another problem was that the Cri data are in the form of radiance values while the FieldSpec Pro data provide reflectance values. We chose to change the targets' spectrum reflectances to radiances for computational simplicity as we then do not have to change the whole imagery. We first measured the spectrum of a "white" object (a standard whiteboard in our experiments); this spectrum was taken as the solar illumination term. Then, the spectrum of the target was measured and the solar illumination term was removed from it to obtain the reflectance of the target. This removal processing was automatically done by the ViewSpec Pro software in the FieldSpec Pro spectroradiometer. This software also could convert the reflectance to radiance, so we just had to convert the reflectance to match the sensor. In addition, we used another way to acquire the targets' radiance in our experiments. We fixed the targets with the same materials but with much
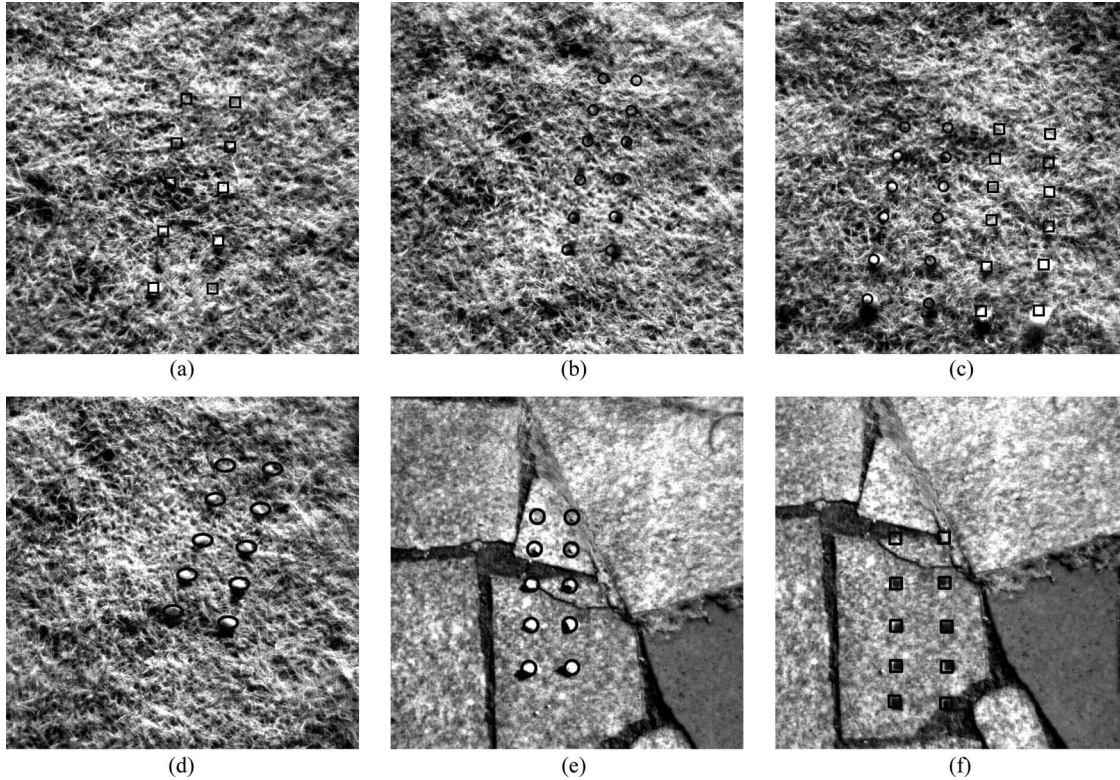
Fig. 3. Cri images in our experiments. (a) Image 1. (b) Image 2. (c) Image 3. (d) Image 4. (e) Image 5. (f) Image 6.

larger scale and imaged another image with our Cri sensor to formulate pure target pixels in the same scenes at the same time. Then, we selected the targets' radiances from the images.

C. Determination and Sensitivity of the Adjust Coefficient

In the new proposed hybrid detectors, the adjustment coefficient η is a very important parameter. It adjusts the selected endmembers' weights in the test pixel. Too low a value would not affect the real abundances of the endmembers, while too high a value would cause the omission of other important endmembers. Moreover, too low a value would also increase the computational burden. Therefore, a suitable value of η should balance the algorithm's speed and the selected endmembers' weights. In our experiments, the synthetic data were used to determine the suitable value of η so that it could be used in the experiments employing simulated data and real-world hyperspectral data. The synthetic data were images composed of several kinds of ground objects' spectrum signatures from the ENVI software spectrum library. We chose five kinds of object spectrum to compose this data: Jasper Ridge grassland soil, Coyote bush, drygrass, lawn grass, and Blackbrush leaves. Their spectrum plots are shown in Fig. 4. We calibrated their spectra to the corresponding bands of Aviris in the overlapping parts of their spectrum and chose 100 bands with high quality. In this way, we obtained five spectrum signatures, which were vectors with a dimension of 100. Then, using similar methods to those in [10], we obtained the synthetic hyperspectral data set composed of these five spectrum signatures. The data set contained 400 pixels, divided into four groups each containing 100 pixels of the same mixture. The first group contained 50% soil and 50% bush. The second group contained 50% bush and 50% grass. The third group contained 50% soil and 50% grass. The fourth
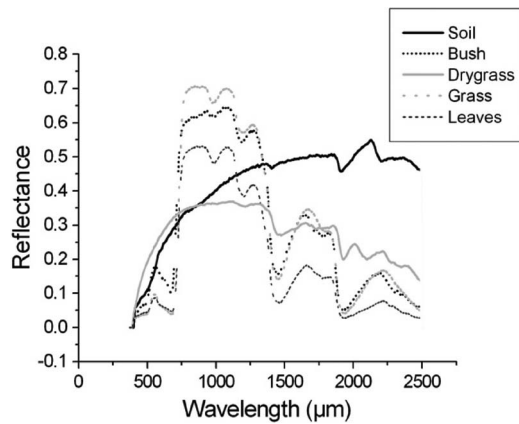

Fig. 4. Reflectance of five signatures.

group contained 50% soil and 50% leaves. Then, we chose the first 25 pixels from each group and added 10% drygrass to them. For example, for the 25 chosen pixels in the first group, we added 10% drygrass and then the abundances of soil and bush were both reduced to 45%. In this way, we obtained 100 subpixel targets of drygrass in the synthetic data set. In addition, we also added Gaussian white noise with an SNR of 30 : 1.

As we know the composition of the synthetic pixels beforehand, we can easily define the selective endmember matrices M_S and M_{BS} by introducing the corresponding actual kinds of endmembers' spectra in the right-hand column. After that, we can use the hybrid selective endmembers detectors in the detection. Considering the HSESD, we changed the value of the adjustment coefficient η from 0.35 to 0.8 with steps of 0.05 and obtained a series of detection results. The probability of detection under different η is shown in Fig. 5. We found that
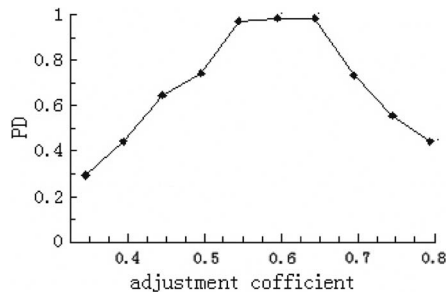
Fig. 5.   Detection rate under different η.

TABLE II
PERFORMANCE OF REMOVING UNNECESSARY ENDMEMBERS I

Endmember	Real number	FCLS	Our method
Bare soil	40	32	35
Grass	30	25	28
Drygrass	32	29	30

TABLE III
PERFORMANCE OF REMOVING UNNECESSARY ENDMEMBERS II

Endmember	Real number	FCLS	Our method
Bare soil	40	38	38
Grass	30	29	28
Drygrass	32	30	30

TABLE IV
PERFORMANCE OF REMOVING UNNECESSARY ENDMEMBERS III

METHOD	NO NOISE	SNR=100:1	SNR=30:1
FCLS	100	90	81
OUR METHOD	100	96	94

as η increases from 0.35 to 0.55, the probability of detection increases significantly from 0.3 to 0.95. However, as η increases from 0.55 to 0.65, the probability of detection almost remains stable. As η increases further above 0.65, the probability of detection begins decreasing. It is inferred that the suitable value of η is in [0.55, 0.65]. In the case of the hybrid selective endmembers unstructured detector, the analysis procedure is similar and the resulting determination of η was [0.54, 0.60]. In the following experiments, we used these numerical ranges for HSESD and HSEUD.

D. Analysis of Endmembers Selection

The main point of this paper is that by selecting the correct endmembers for a particular pixel out of the entire endmember matrix will improve subpixel target detection performance. However, FCLS can promote sparsity when calculating abundances, and many of the abundances are driven to zero automatically, which essentially does the same thing as selecting the correct endmembers from an endmember matrix. Therefore, what would be convincing would be some experiments comparing the endmembers selection using FCLS with the proposed method. We choose 100 pixels from the Cri image 1 and get definite composition of endmembers in each pixel from field work. The real numbers of pixels not containing certain endmembers (unnecessary endmembers) are listed in the second column of Table II. We use FCLS to find the number of zero abundance for each unnecessary endmember and use our method to calculate the number of the removals of each unnecessary endmember in these pixels. Both results are listed in the last two columns of Table II. Our method performs obviously better than that of FCLS.

In the aforementioned experiment, we use the most optimal endmembers estimated from IEA. However, since we have exact ground true information, we also use the endmembers' spectrums selected from the pure pixels in the image. Then, the results are listed in Table III. This time, FCLS has little difference with our method. Therefore, we can conclude that FCLS's performance of removing unnecessary endmembers is sensitive to the accuracy of the endmembers' spectrums. As to the target detection practice, since the estimation of background endmembers can be only done to a certain degree, our method

would be more practical than FCLS in removing unnecessary endmembers.

Additionally, we investigate effect of noise in hyperspectral imagery to the removal of unnecessary endmembers. This time, we use the same synthetic data with that in this paper. In addition, we synthesize other two images by the same method but one with no additional Gaussian noise, the other with an SNR of 100 : 1. We choose 100 pixels, none of which contains bush, and investigate their removal performances of bush and list them in Table IV. It shows in Table IV that with more noise FCLS presents less number of zero abundances which indicates its sensitivity to noise. Meanwhile, our method is not so sensitive to noise.

Above all, since we cannot avoid from estimation error of background endmembers and the noise effect in the imagery, ours seems to be more promising than FCLS in removing the unnecessary endmembers.

E. Detection Results

Under the optimal case, we can estimate the correct number of endmembers in the image. In this case, it is expected that all the hybrid detectors will output the best results for the separation of targets and background. Since we have real data concerning the ground targets, we can accurately estimate the number of endmembers. We first compared the results of these hybrid detectors with the accurate number of endmembers. The detection results of Cri Image 2 are shown in Fig. 6, which shows that all the hybrid detectors performed well since each of them can attain a target detection of 100%. The only difference is the number of false alarms. However, all of the hybrid detectors suppress the number of false alarm to under two. Moreover, the detection results of other Cri images and of the PHI data also show that all the hybrid detectors can detect 100% of the targets with a similar low number of false alarms, which is shown in Table V. That is to say, there is hardly any difference in performance between these hybrid detectors.

F. Endmember Sensitivity Analyses

In practical detection, it is difficult to determine the accurate number of endmembers in the imaging scene. We have to resort to algorithms to estimate it [19]. However, underestimation or overestimation of the number of endmembers is unavoidable. In order to implement our proposed algorithms in the real-world detection environment, we would need to evaluate their sensitivity to varying numbers of endmembers. We first took the PHI simulated imagery into consideration. The choice of
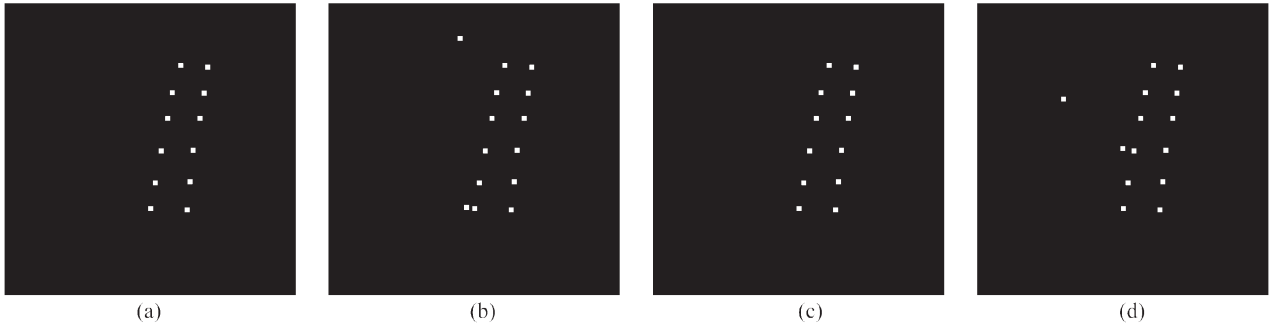
Fig. 6.   Detection results of hybrid detectors using Cri Image 2. (a) HSD. (b) HUD. (c) HSESD. (d) HSEUD.

TABLE   V
NUMBER OF FALSE ALARMS FOR HYBRID DETECTORS

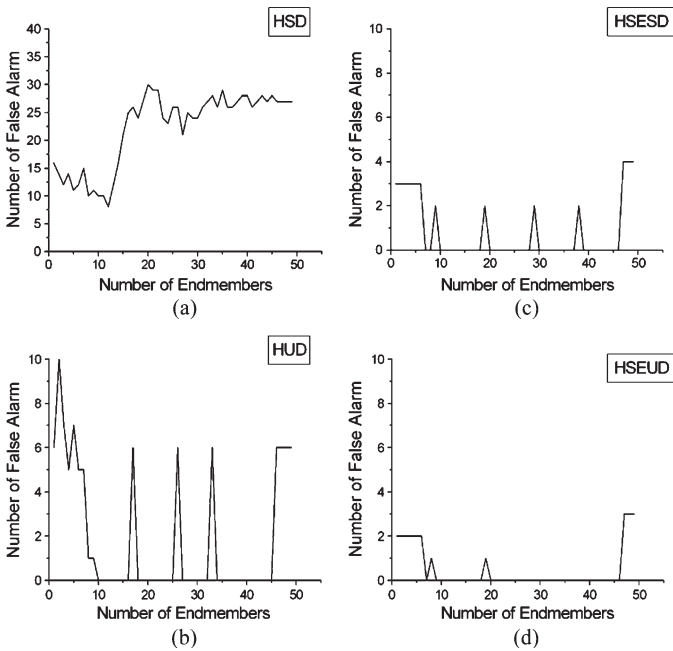| IMAGE	HSD	HUD	HSESD	HSEUD
1	1	2	0	2
2	0	2	0	2
3	1	1	1	1
4	0	0	0	0
5	0	0	0	0
6	0	0	0	0
PHI	0	1	0	1

Fig. 7.   False alarm rates versus number of endmembers. (a) HSD. (b) HUD. (c) HSESD. (d) HSEUD.

this imagery is due to there being enough prior information concerning the ground truth. We had detailed information about the land cover types in the imaging scene, and we found that there were 12 main kinds of ground objects. In addition, the complexity of the land objects makes it approximate to a real-world detection application. In the experiments, we changed the number of endmembers from 1 to 55 and applied the HSD, HUD, HSESD, and HSEUD to the PHI simulated data. Then, by fixing the probability of detection to 100%, we obtained a series of numbers of false alarms. Fig. 7 shows the number of false alarms of the three detectors when the number of endmem-

bers varies from 1 to 55. In the experiments, all the algorithms showed a steady downward trend approaching the number 55 and this trend continues above that number. Therefore, we did not take numbers above 55 into consideration.

It is shown in Fig. 7 that HSD shows a most irregular distribution of the number of false alarms. HUD does well in the detection, as the number of false alarms is well under ten across the whole range. In addition, when the number of endmembers is above ten, the number of false alarms is regular, which indicates a good insensitivity to a variation in the number of endmembers. However, when the number of endmembers is under ten, the values of false alarms are somewhat random and even a minor change in the number of endmembers would cause a distinct change in false alarms, which vary from zero to ten. HSESD and HSEUD both show a regular trend no matter whether the number of endmembers is under ten or not. Moreover, their numbers of false alarms are below five over the whole range, while the number of false alarms of HUD exceeds five several times over the range and HSD exceeds five most times. That is to say, the proposed HSESD and HSEUD are even more insensitive to the number of endmembers than HUD. Fig. 7 also shows that HESUD does best among the three. This is very interesting as it is revealed in [18] that the hybrid unstructured detector is more insensitive to the number of endmembers than the structured hybrid detector. Therefore, our detection results concerning endmember sensitivity also prove that the removal of background structured information enhances the insensitivity to the number of endmembers. From the ground truth information, we know that there are no more than 12 kinds of ground objects. However, the number of subclasses is much larger. For example, the class of Roads has as many as 35 subclasses, some of which have similar spectral features to those of the targets. When the number of endmembers was taken as under ten, these subclasses were mixed together, which made them difficult to separate from the targets and caused more false alarms. Fig. 7 shows that both HSESD and HSEUD overcame this limitation.

To evaluate the algorithms' sensitivity to endmember numbers for different targets with different backgrounds, we also inspected the detection results of Cri hyperspectral imageries. This time we calculated the frequency of occurrence of the best detection results as the number of endmembers varied from 2 to 20. The best performances are defined as a probability of detection approximating 100% with a FAR as low as possible. The larger the frequency, the more insensitive is the algorithm. The number of 20 was chosen as the upper boundary due to the obvious downward trend of all three algorithms when the

TABLE VI
NUMBER OF FALSE ALARMS FOR HYBRID DETECTORS

TARGET	IMAGE	BACKGROUND	HSD	HUD	HSESD	HSEUD
PLASTIC	1	BARE SOIL, GRASS, DRY GRASS	6	9	10	17
	2	BARE SOIL, GRASS, DRY GRASS				
	3	BARE SOIL, GRASS, DRY GRASS	4	8	10	16
	4	BARE SOIL, GRASS, DRY GRASS				
	5	BARE SOIL, CEMENT				
	6	BARE SOIL, CEMENT	14	16	17	19
METAL	1	BARE SOIL, GRASS, DRY GRASS				
	2	BARE SOIL, GRASS, DRY GRASS	11	13	14	18
	3	BARE SOIL, GRASS, DRY GRASS	9	10	11	17
	4	BARE SOIL, GRASS, DRY GRASS				
	5	BARE SOIL, CEMENT	17	19	19	20
	6	BARE SOIL, CEMENT				
STONE	1	BARE SOIL, GRASS, DRY GRASS				
	2	BARE SOIL, GRASS, DRY GRASS				
	3	BARE SOIL, GRASS, DRY GRASS				
	4	BARE SOIL, GRASS, DRY GRASS	10	15	16	20
	5	BARE SOIL, CEMENT				
	6	BARE SOIL, CEMENT				

number of endmembers approached 20. The number of ground objects is much lower than in the PHI imagery as the imaging range is much smaller, so the best number of endmembers is also dramatically reduced. Table VI shows the numbers of the best performances of the three kinds of targets in six images. The gray cells mean that the according imagery in the same row does not contain the target. In addition, the occurrence numbers of the best performance of HSD, HUD, HSEED, and HSEUD for a particular kind of target in these images are listed in the right parts of the rows.

Images 5 and 6 are the easiest ones among the six images. That is because all the targets in them were positioned on a plane and simple background. The background was composed of bare soil and cement, which were not overlapping with and none of the targets were hidden by the background. The other four images are more difficult, not only because their backgrounds were composed of more ground objects but also because the background ground objects were uneven, which caused partial hiding of targets. Among the other four images, Image 3 is the most difficult because there were more kinds of target in it and more targets were hidden. Table VII shows the number of targets that were partially hidden by the background in these six images. From Table VII, we find that for Image 5 and Image 6 the three hybrid detectors all performed well with a number near 20. However, as the images become more difficult, these detectors performed differently. HSD performs worst among the four detectors. HUD shows a lower number than HSESD and HSEUD in Image 2, and the performance of HUD reduces to under ten in Image 1 and Image 3. Meanwhile,

TABLE VII
NUMBER OF PARTIALLY HIDDEN TARGETS

IMAGE NUMBER	TARGET KIND	TARGET NUMBER	NUMBER OF TARGETS PARTIALLY HIDDEN
1	PLASTIC	10	4
2	METAL	12	3
3	PLASTIC	12	6
	METAL	12	5
4	STONE	10	2
5	METAL	10	0
6	PLASTIC	10	0

HSESD and HSEUD both keep a higher number in these two images and HSEUD performs best. Above all, these experimental results again indicate that HSESD and HSEUD are more insensitive to the number of endmembers than are HSD and HUD.

G. Separability Analysis

In our experiments, we found all the hybrid detectors performed well as measured by the probability of detection. However, following the work of [3], we know that a good algorithm would present a better separability between targets and background. In addition, a robust detector with better separability is defined as one to show a steadily suppressed background through all images. In the same way as [3], we analyzed the detecting results for different images with different hybrid detectors and calculated the targets' and background's statistical ranges. For each detector, there are six groups of bars in the graph, which accord to the six Cri images. Except for
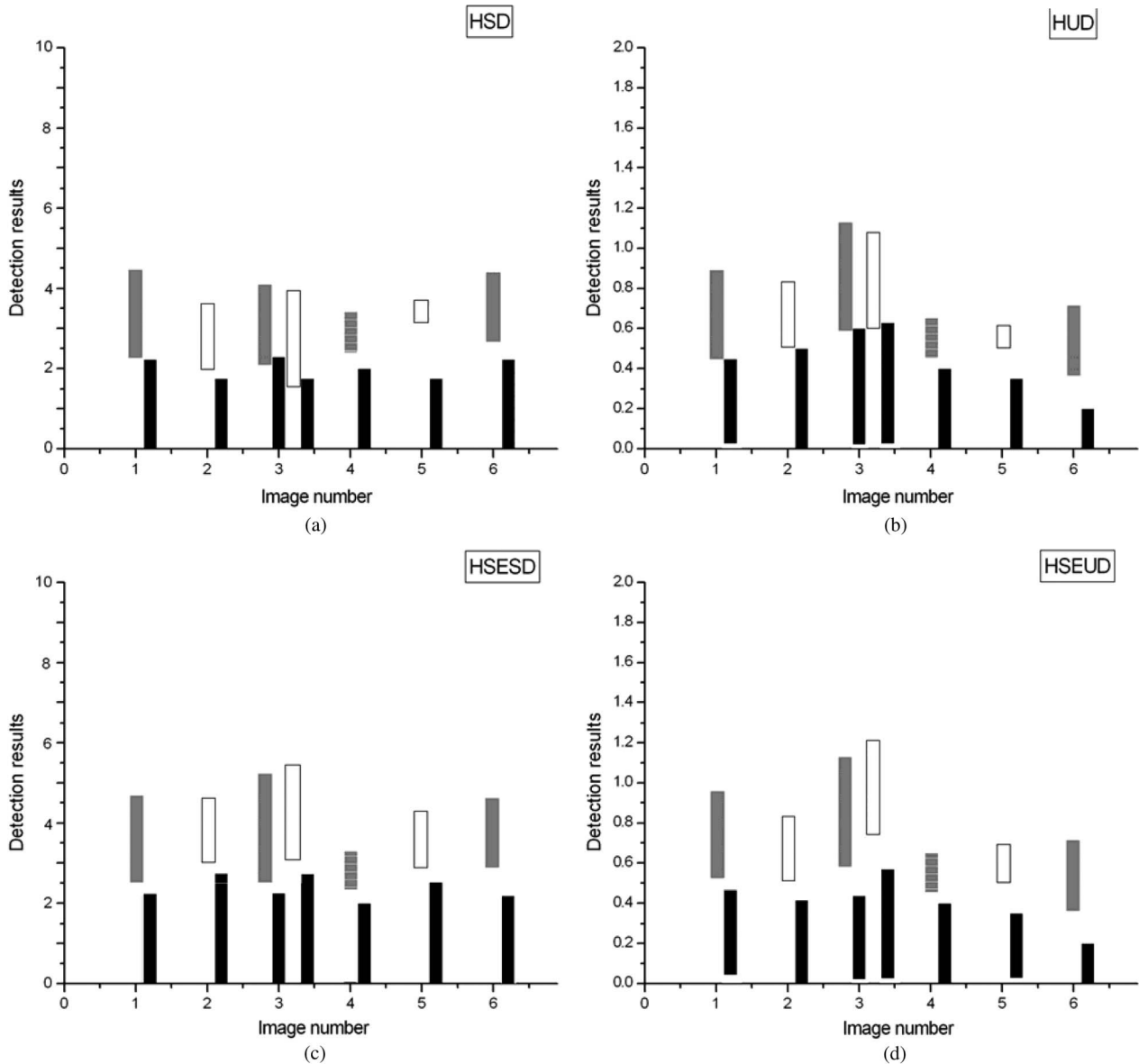
Fig. 8. Separability analysis of four hybrid detectors. (a) HSD. (b) HUD. (c) HSESD. (d) HSEUD.

Group 3, each contains two bars: the target on the left and the background on the right. Group 3 has four bars as it has two kinds of target and two backgrounds. All the background bars are colored black and the targets have different colors according to their kind: plastic is gray, metal is white, and stone is black alternating with white. Fig. 8 shows the separability differences for these images. Considering Image 4, Image, 5 and Image 6, all the detectors perform well since there is an obvious gap between the target bar and the background bar for each of them. However, these three images are the comparatively easy ones since the targets are rarely overlapping their backgrounds and their spectra are distinct from the background. Referring to the more difficult ones, things begin distinctly. For Image 2, HUD shows an obscure gap between target bar and background bar, while the other three hybrid detectors keep sufficient gaps. For Image 1, HUD presented two false alarms and HSD presents an obscure gap. Meanwhile, HSEUD and HSESD still present satisfactory separability. For Image 3, the separability differences are much larger. Since Image 3 has two kinds of target, which means more spectral variety, and has most hidden targets, this

makes it the most difficult one. Both HSD and HUD exhibit obvious overlap between target and background, while HSESD and HSEUD still have discriminatable gaps.

We also analyzed the background range, which suggests the performance of suppressing the background. A good performance is one suppressing the background into the same range across images. This time, the same kind of targets and their background are taken into consideration. First, the targets of plastic are referred to, represented by the gray bars in Fig. 8. All the hybrid detectors suppressed the background of plastic to a low value. However, both HSD and HSESD suppress the background to nearly the same range across Images 1, 3, and 6, while the unstructured ones HUD and HSEUD provide a comparable irregular background range. Secondly, for targets of metal (white bars in Fig. 8), the same conclusion can be drawn. Although the HSEUD suppresses the background into a comparable fluctuating range, the range of the background is obviously smaller than with the other three. Above all, the hybrid detectors based on selective endmembers show better separability than the conventional hybrid detectors.
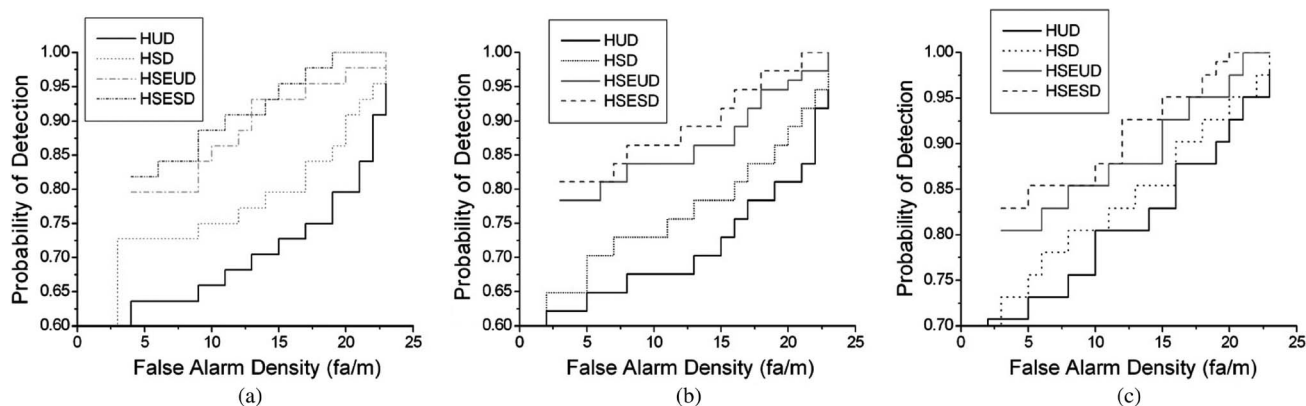
Fig. 9. ROC curves for hybrid detectors. (a) Metal. (b) Stone. (c) Plastic.

H. ROCs Analysis

The CFAR detector is one of the most important methods in subpixel target detection whose property is often measured by ROCs curves. Reference [19] has shown that the conventional structured and unstructured hybrid detectors have a property similar to the CFAR detector. It is easily concluded that the hybrid detectors based on selective endmembers also have such a property, since the only difference is that the new proposed hybrid detectors introduce a more reasonable background structure than the conventional hybrid detectors. Following the work of [19], we further analyzed the CFAR-like property of the proposed hybrid detectors by ROC curves. In our experiments, as the number of targets is small, we added two other images containing 27 stone targets, 10 metal targets, and 9 plastic targets altogether, and the total number of the three kinds of targets are 37, 44, and 41, respectively. Then, we calculated the total statistics of different hybrid detectors for each kind of targets in all the images with successive thresholds and plotted the ROC curves.

Fig. 9(a)–(c) shows the ROC curves for the three different kinds of targets: metal, stone, and plastic. It is revealed that our proposed hybrid detectors lie on top of the conventional hybrid detectors in all the figures. However, due to the paucity of targets, the generated ROC curves improvement would not be statistically significant. Moreover, the stricter method is to evaluate the corresponding confidence bands of the ROC curves for different detectors. The best detector should have confidence bands nearest to the upper-left and with little overlap with the other detectors' confidence bands in ROC space. There are many methods of constructing the confidence bands for ROC curves, which is beyond our research focus in this paper. Nevertheless, Fig. 9 shows our proposed hybrid detectors are CFAR-like, and are useful for ROC analysis.

V. CONCLUSION

In this paper, we further investigated the background's real composition of endmembers for each pixel and introduced the endmembers selection information into the hybrid detectors to develop the hybrid selective endmembers detectors. With the selective endmembers for each pixel, the proposed hybrid detectors characterize the background according to reality. A background modeled with the selected dynamic endmembers is assumed to be characterized better than the traditional strategy with fixed endmembers and conforms to reality. Experiments

reveal that the hybrid selective endmembers detectors are even more insensitive to changes in the endmembers' number, particularly in the case when the endmembers' number is underestimated, which is the special superiority of our proposed hybrid detectors. That is to say, our proposed hybrid detectors can overcome the inexact estimation of endmembers, which is the usual case in practical detection. The hybrid selective endmembers detectors also have better separability than conventional hybrid detectors and suppress the background consistently across images. They even show a considerable separability when the target's spectrum and the background's spectrum are very similar, while the conventional hybrid detectors show a dramatic decrease as the targets become more similar to their background. The last measurement for the hybrid selective endmembers detectors is the CFAR property, which is presented by the ROC curve. Another important improvement is that the hybrid selective endmembers detectors have overcome the inevitable reduction of performance when the targets become more similar to the background, as shown in [19]. However, endmembers in each pixel need to be accurately identified in our proposed approach; otherwise, the inaccurate identification of endmembers will cause poor detection results. That is the limitation of our methods. Moreover, research still needs to be done on the endmember selection since correlation coefficient-based method is not the best method in providing per-pixel endmember selection. In addition, those are the focus of our future work.

REFERENCES

[1] C.-I Chang, *Hyperspectral Imaging: Spectral Detection and Classification*. New York: Plenum, 2003.
[2] H. Ren and C.-I Chang, "Automatic spectral target recognition in hyperspectral imagery," *IEEE Trans. Aerosp. Electron. Syst.*, vol. 39, no. 4, pp. 1232–1249, Oct. 2003.
[3] D. Manolakis, D. Marden, and G. A. Shaw, "Hyperspectral image processing for automatic target detection applications," *Lincoln Lab. J.*, vol. 14, no. 1, pp. 79–116, 2003.
[4] D. Manolakis and G. Shaw, "Detection algorithms for hyperspectral imaging applications," *IEEE Signal Process. Mag.*, vol. 19, no. 1, pp. 29–43, Jan. 2002.
[5] X. Huang and L. Zhang, "An adaptive mean-shift analysis approach for object extraction and classification from urban hyperspectral imagery," *IEEE Trans. Geosci. Remote Sens.*, vol. 46, no. 12, pp. 4173–4185, Dec. 2008.
[6] X. Huang, L. Zhang, and P. Li, "Classification and extraction of spatial features in urban areas using high resolution multispectral imagery," *IEEE Geosci. Remote Sens. Lett.*, vol. 4, no. 2, pp. 260–264, Apr. 2007.
[7] Q. Du, "Optimal linear unmixing for hyperspectral image analysis," in *Proc. IEEE IGARSS*, 2004, vol. 5, pp. 3219–3221.

[8] D. C. Heinz and C.-I Chang, "Fully constrained least squares linear spectral mixture analysis method for material quantification in hyperspectral imagery," *IEEE Trans. Geosci. Remote Sens.*, vol. 39, no. 3, pp. 529–545, Mar. 2001.

[9] D. Manolakis, C. Siracusa, and G. Shaw, "Hyperspectral subpixel target detection using the linear mixing model," *IEEE Trans. Geosci. Remote Sens.*, vol. 39, no. 7, pp. 1392–1409, Jul. 2001.

[10] C.-I Chang and D. C. Heinz, "Constrained subpixel target detection for remotely sensed imagery," *IEEE Trans. Geosci. Remote Sens.*, vol. 38, no. 3, pp. 1144–1159, May 2000.

[11] Y. E. Shimabukuro and J. A. Smith, "The least squares mixing models to generate fraction images derived from remote sensing multispectral data," *IEEE Trans. Geosci. Remote Sens.*, vol. 29, no. 1, pp. 16–20, Jan. 1991.

[12] J. Li, "Linear unmixing of hyperspectral signals via wavelet feature extraction," Ph.D. dissertation, Mississippi State Univ., Mississippi State, MS, 2002.

[13] S. Jia and Y. Qian, "Constrained nonnegative matrix factorization for hyperspectral unmixing," *IEEE Trans. Geosci. Remote Sens.*, vol. 47, no. 1, pp. 161–173, Jan. 2009.

[14] D. Heinz, C.-I Chang, and M. L. G. Althouse, "Fully constrained least-squares based linear unmixing [hyperspectral image classification]," in *Proc. IEEE IGARSS*, 1999, vol. 2, pp. 1401–1403.

[15] Q. Du, L. Wasson, and R. King, "Unsupervised linear unmixing for change detection in multitemporal airborne hyperspectral imagery," in *Proc. Int. Workshop Anal. Multi-Temporal Remote Sens. Images*, 2005, pp. 136–140.

[16] B. Thai and G. Healey, "Invariant subpixel material detection in hyperspectral imagery," *IEEE Trans. Geosci. Remote Sens.*, vol. 40, no. 3, pp. 599–608, Mar. 2002.

[17] Q. Du and C.-I Chang, "A signal-decomposed and interference-annihilated approach to hyperspectral target detection," *IEEE Trans. Geosci. Remote Sens.*, vol. 42, no. 2, pp. 892–906, Apr. 2004.

[18] S. Kraut, L. L. Scharf, and R. W. Butler, "The adaptive coherence estimator: A uniformly most-powerful-invariant adaptive detection statistic," *IEEE Trans. Signal Process.*, vol. 53, no. 2, pp. 427–438, Feb. 2005.

[19] J. Broadwater and R. Chellappa, "Hybrid detectors for subpixel targets," *IEEE Trans. Pattern Anal. Mach. Intell.*, vol. 29, no. 11, pp. 1891–1903, Nov. 2007.

[20] J. Broadwater and R. Chellappa, "A hybrid algorithm for subpixel detection in hyperspectral imagery," in *Proc. IEEE IGARSS*, 2004, vol. 3, pp. 1601–1604.

[21] C. Ichoku and A. Karnieli, "A review of modeling technique for sub-pixel land cover estimation," *Remote Sens. Rev.*, vol. 13, no. 3/4, pp. 161–186, Apr. 1996.

[22] N. Keshava and J. F. Mustard, "Spectral unmixing," *IEEE Signal Process. Mag.*, vol. 19, no. 1, pp. 44–57, Jan. 2002.

[23] J. Settle and N. A. Drake, "Linear mixing and estimation of ground cover proportions," *Int. J. Remote Sens.*, vol. 14, no. 6, pp. 1159–1177, Apr. 1993.

[24] E. A. Ashton and A. Schaum, "Algorithms for the detection of subpixel targets in multispectral imagery," *Photogramm. Eng. Remote Sens.*, vol. 64, no. 7, pp. 723–731, Jul. 1998.

[25] D. Heinz, C.-I Chang, and M. L. G. Althouse, "Fully constrained least squares-based linear unmixing," in *Proc. Int. Geosci. Remote Sens. Symp.*, Hamburg, Germany, 1999, pp. 1401–1403.

[26] C.-I Chang, X. Zhao, M. L. G. Althouse, and J.-J. Pan, "Least squares subspace projection approach to mixed pixel classification in hyperspectral images," *IEEE Trans. Geosci. Remote Sens.*, vol. 36, no. 3, pp. 898–912, May 1998.

[27] T. M. Tu, C.-H. Chen, and C.-I Chang, "A least squares orthogonal subspace projection approach to desired signature extraction and detection," *IEEE Trans. Geosci. Remote Sens.*, vol. 35, no. 1, pp. 127–139, Jan. 1997.

[28] S. M. Kay, *Fundamentals of Statistical Signal Processing*. Englewood Cliffs, NJ: Prentice-Hall, 1998.

[29] R. Gnanadesikan, *Methods for Statistical Data Analysis of Multivariate Observations*. New York: Wiley, 1997.

[30] E. J. Kelly, "An adaptive detection algorithm," *IEEE Trans. Aerosp. Electron. Syst.*, vol. AES-22, no. 2, pp. 115–127, Mar. 1986.

[31] E. J. Kelly, "Adaptive detection in non-stationary interference, part III," MIT Lincoln Lab., Lexington, MA, 1987.

[32] E. J. Kelly and K. M. Forsythe, "Adaptive detection and parameter estimation for multidimensional signal models," MIT Lincoln Lab., Lexington, MA, Apr. 1989.

[33] I. S. Reed and X. Yu, "Adaptive multiple-band CFAR detection of an optical pattern with unknown spectral distribution," *IEEE Trans. Acoust., Speech, Signal Process.*, vol. 38, no. 10, pp. 1760–1770, Oct. 1990.

[34] D. Stein, S. Beaven, L. Hoff, E. Winter, A. Schaum, and A. Stocker, "Anomaly detection from hyperspectral imagery," *IEEE Signal Process. Mag.*, vol. 19, no. 1, pp. 58–69, Jan. 2002.

[35] C.-I Chang and Q. Du, "Estimation of number of spectrally distinct signal sources in hyperspectral imagery," *IEEE Trans. Geosci. Remote Sens.*, vol. 42, no. 3, pp. 608–619, Mar. 2004.

[36] D. A. Roberts, M. Gardner, R. Church, S. Ustin, G. Scheer, and R. O. Green, "Mapping chaparral in the Santa Monica Mountains using multiple endmember spectral mixture models," *Remote Sens. Environ.*, vol. 65, no. 3, pp. 267–279, Sep. 1998.

[37] V. F. Meer and W. Bakker, "CCSM: Cross correlogram spectral matching," *Int. J. Remote Sens.*, vol. 18, no. 5, pp. 1197–1201, 1997.

[38] P. J. Martínez, R. M. Pérez, A. Plaza, P. L. Aguilar, M. C. Cantero, and J. Plaza, "Endmember extraction algorithms from hyperspectral images," *Ann. Geophys.*, vol. 49, no. 1, pp. 93–101, Feb. 2006.

[39] A. M. Filippi and R. Archibald, "Support vector machine-based endmember extraction," *IEEE Trans. Geosci. Remote Sens.*, vol. 47, no. 3, pp. 771–791, Mar. 2009.

[40] R. A. Neville, K. Staenz, T. Szeredi, J. Lefebvre, and P. Hauff, "Automatic endmember extraction from hyperspectral data for mineral exploration," in *Proc. 4th Int. Airborne Remote Sens. Conf. Exhib./21st Can. Symp. Remote Sens.*, Ottawa, ON, Canada, 1999, vol. 2, pp. 891–897.

Liangpei Zhang received the B.S. degree in physics from Hunan Normal University, ChangSha, China, in 1982, the M.S. degree in optics from the Xi'an Institute of Optics and Precision Mechanics, Chinese Academy of Sciences, Xi'an, China, in 1988, and the Ph.D. degree in photogrammetry and remote sensing from Wuhan University, Wuhan, China, in 1998.

He is currently with the State Key Laboratory of Information Engineering in Surveying, Mapping and Remote Sensing, Wuhan University, as the Head of the Remote Sensing Division. He is also a "Chang-Jiang Scholar" Chair Professor appointed by the Ministry of Education, China. He has more than 180 research papers and five patents. His research interests include hyperspectral remote sensing, high-resolution remote sensing, image processing, and artificial intelligence.

Dr. Zhang is a Fellow of Institution of Electrical Engineers, Executive Member (Board of Governor) of the China National Committee of International Geosphere-Biosphere Program, Executive Member for the China Society of Image and Graphics, and others. He regularly serves as a Cochair of the series SPIE Conferences on Multispectral Image Processing and Pattern Recognition, Conference on Asia Remote Sensing, and many other conferences. He edits several conference proceedings, issues, and the Geoinformatics Symposiums. He also serves as an Associate Editor of the *International Journal of Ambient Computing and Intelligence*, *International Journal of Image and Graphics*, *Journal of Geo-spatial Information Science*, and the *Journal of Remote Sensing*.

Bo Du received the B.S. and M.S. degrees in graphic engineering from Wuhan University, Wuhan, China, in 2005 and 2007, respectively, where he is currently working toward the Ph.D. degree in the State Key Laboratory of Information Engineering in Surveying, Mapping and Remote Sensing, Wuhan University.

His major research interests include hyperspectral image processing, signal processing, and pattern recognition.
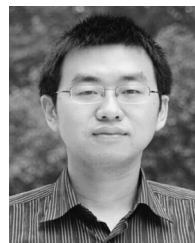
Yanfei Zhong received the B.S. degree in information engineering and the Ph.D. degree in photogrammetry and remote sensing from Wuhan University, Wuhan, China, in 2002 and 2007, respectively.

He is currently an Associate Professor with the State Key Laboratory of Information Engineering in Surveying, Mapping and Remote Sensing, Wuhan University. His major research interests include multi- and hyperspectral image processing, artificial intelligence, and pattern recognition.